Journal of Non-Newtonian Fluid Mechanics 187–188 (2012) 16–31

Contents lists available at SciVerse ScienceDirect

Journal of Non-Newtonian Fluid Mechanics

journal homepage: http://www.elsevier.com/locate/jnnfm

# The Free (Open) Boundary Condition at inflow boundaries

Yannis Dimakopoulos [a], George Karapetsas [b], Nikolaos A. Malamataris [c,d], Evan Mitsoulis [e,*]

[a] Department of Chemical Engineering, University of Patras, Rion 265 00, Greece
[b] Department of Mechanical Engineering, University of Thessaly, GR-38334 Volos, Greece
[c] Department of Mechanical Engineering, TEI of Western Macedonia, GR-50100 Kila-Kozani, Greece
[d] Department of Computational and Data Sciences, George Mason University, Fairfax, VA 22030, USA
[e] School of Mining Engineering & Metallurgy, National Technical University of Athens, Zografou, 157 80 Athens, Greece

ARTICLE INFO

*Article history:*
Received 29 May 2012
Received in revised form 31 July 2012
Accepted 2 September 2012
Available online 10 September 2012

*Keywords:*
Free (Open) Boundary Condition (FBC, OBC)
Inflow boundary condition
Viscous flow
Viscoelastic flow
Non-Newtonian fluids

ABSTRACT

The Free (or Open) Boundary Condition (FBC, OBC) was proposed by Papanastasiou et al. (A new outflow boundary condition, Int. J. Numer. Meth. Fluids 14 (1992) 587–608) to handle truncated domains with synthetic boundaries where the outflow conditions are unknown. In the present work, implementation of the FBC has been tested also at *inflow boundaries* in several test problems of viscous or viscoelastic flow. The Finite Element Method (FEM) is used to provide numerical results for both cases of planar and axisymmetric domains under laminar, isothermal or non-isothermal, steady-state conditions for Newtonian and non-Newtonian fluids. The present results extend previous ones regarding the applicability of the FBC, since they convincingly show that the FBC can be used equally well at inflow boundaries, without having to resort to artificially set inlet profiles for a given flow rate.



## 1. Introduction

The Free (Open) Boundary Condition (FBC, OBC) was proposed by Papanastasiou et al. [1] to handle truncated domains with synthetic boundaries where the outflow conditions are unknown. Since then, a number of works have used the FBC in a variety of flow problems [2–12]. A recent paper [13] has revisited the FBC and showed its proper use in some viscous flow problems including free surfaces. The work was extended to viscoelastic flow simulations with differential [14] or integral models [15] with equally good results.

It has been argued that the FBC works well because in essence it is a projection or an extrapolation of the flow field equations to the outflow boundary [1,8]. In that sense, it must also work at the inflow boundary, where usually arbitrary and/or simple boundary conditions are imposed. In most cases, a fully developed velocity profile is imposed far upstream that corresponds to the fluid model at hand. If there is no analytical solution, usually a one-dimensional (1D) numerical solution is imposed [16,17]. In other cases and in several commercial codes, the simplest way to handle inflow boundary conditions is to impose a plug profile corresponding to a given flow rate, and then let the solution develop and take the correct profile some distance away from the inflow. In all these cases, the flow field near the inflow boundary is not well behaved when there are nonlinear phenomena, and something else is needed to take care of the uncertainty at the inflow.

Issues regarding inflow boundary conditions arise when the inflow is not fixed, due to the fact that there is no clear entrance of the flow. Applications of this situation appear in biomedical flows where the focus of observation is in a part of a body where the flow of blood is continuous and the entrance is the synthetic inlet that is created from the window of observation. The subject matter is an active research topic as evidenced by some very recent publications on the subject [18,19]. Other applications include polymer flows, where the non-Newtonian viscoelastic character of the fluids flowing inside complicated polymer processing equipment may make the inlet not clearly defined [20,21].

The idea to use the FBC at the inflow as well was first proposed and used by Dimakopoulos et al. [22] to handle blood flow in an aorta at very high Reynolds numbers and using a nonlinear viscous model (the Carreau–Yasuda model). It was shown that the imposition of FBC at the inflow as well as the outflow gave very good numerical results without any oscillations or unrealistic velocity and pressure profiles. It became then obvious that this idea of imposing the FBC at the inlet is worth studying in more detail and applying it to some standard or simple test problems to observe its behavior.

It is therefore the purpose of the present work to impose the FBC at inflow and test it in several problems of Fluid Mechanics with a variety of rheological models, namely viscous, pseudoplastic, viscoplastic, and viscoelastic non-Newtonian models. Apart

* Corresponding author. Tel.: +30 210 772 2163; fax: +30 210 772 2251.
*E-mail address:* mitsouli@metal.ntua.gr (E. Mitsoulis).

0377-0257/$ - see front matter © 2012 Elsevier B.V. All rights reserved.
http://dx.doi.org/10.1016/j.jnnfm.2012.09.001

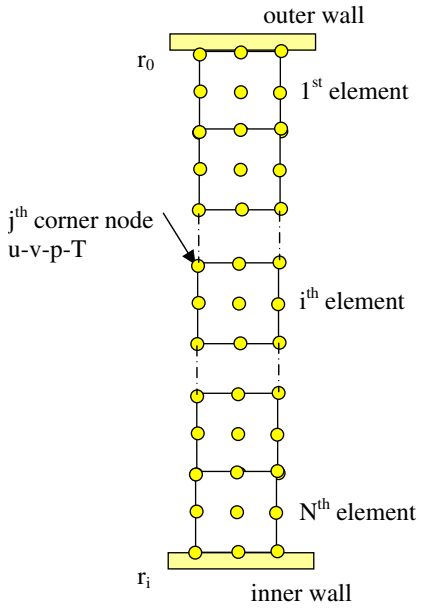


**Fig. 1.** Implementation of the FBC at the inlet boundary. The *j*th corner node of the *i*th element has the *u*-degree of freedom replaced by Eq. (40). For the rest of the inlet boundary nodes, the FBC is applied. Note that for viscoelastic flows each quadrilateral element is split into two triangular elements.

from the work by Dimakopoulos et al. [22], it appears that no other attempt has been made so far in the literature, and this is an effort to examine the implementation and usefulness of FBC as an inflow boundary condition in several problems. The Finite Element Method (FEM) is used to provide and compare numerical results with either analytical solutions or numerical solutions obtained from long domains. Particular emphasis has been placed on truncated domains with flows coming in at an angle.

## 2. Mathematical modelling

### 2.1. Governing equations

Many flowing materials are non-Newtonian, exhibiting either *pseudoplastic* (shear-thinning or -thickening) or *viscoplastic* (presence of a yield stress) behavior or *viscoelastic* behavior [23].

For viscous, compressible or incompressible, steady-state flows, the conservation equations are written as:

- Mass conservation (including density changes for compressible fluids).

$$\nabla \cdot (\rho \bar{u}) = 0. \tag{1}$$

- Momentum conservation (including effects of inertia, pressure, viscous and gravity forces).

$$\rho \bar{u} \cdot \nabla \bar{u} = -\nabla p + \nabla \cdot \bar{\bar{\tau}} + \rho \bar{g}. \tag{2}$$

- Energy conservation (including effects of convection, conduction or diffusion and viscous dissipation).

$$\rho c_p \bar{u} \cdot \nabla T = k \nabla^2 T + \bar{\bar{\tau}} : \nabla \bar{u}. \tag{3}$$

In the above, the field variables are the velocity vector $\bar{u}$, the scalar pressure $p$, the extra stress tensor $\bar{\bar{\tau}}$, and the scalar temperature $T$. The material properties are the density $\rho$, the heat capacity $c_p$, and the thermal conductivity $k$. The acceleration of gravity is $\bar{g}$.

For compressible fluids, we have:

$$\bar{\bar{\tau}} = \mu(\nabla \bar{u} + \nabla \bar{u}^T) - \frac{2}{3}\mu(\nabla \cdot \bar{u})\bar{\bar{I}}. \tag{4}$$

In the above, $\mu$ is a constant viscosity and $\bar{\bar{I}}$ is the unit tensor. Here we have assumed that we deal with dense fluids, which have a zero dilatational (bulk) viscosity [23].

Also for compressible fluids, density and pressure are related via a simple thermodynamic equation of state [23]. Its linear form is given by:

$$\rho = 1 + \beta_c p, \tag{5}$$

where $\beta_c$ is the isothermal compressibility coefficient.

Similarly, the viscosity $\mu$ can be a function of pressure [23]. Its exponential form is given by:

$$\mu = \exp(\beta_p p), \tag{6}$$

where $\beta_p$ is the pressure-shift coefficient.

Along the wall, a slip boundary condition may be occurring [23]. Its linear form is given by:

$$\bar{t} \cdot \bar{u} = \beta_{sl}(\bar{t}\bar{n} : \bar{\bar{\tau}}), \tag{7}$$

where $\beta_{sl}$ is the slip coefficient and $\bar{n}$ and $\bar{t}$ are the normal and tangential unit vectors to the wall.

In 2-D flow problems, it is customary to also use *a posteriori* the Poisson equation for the stream function, the solution of which gives contours of the stream function (streamlines) to help visualize the flow field [23]. The governing equation for the stream function $\psi$ is:

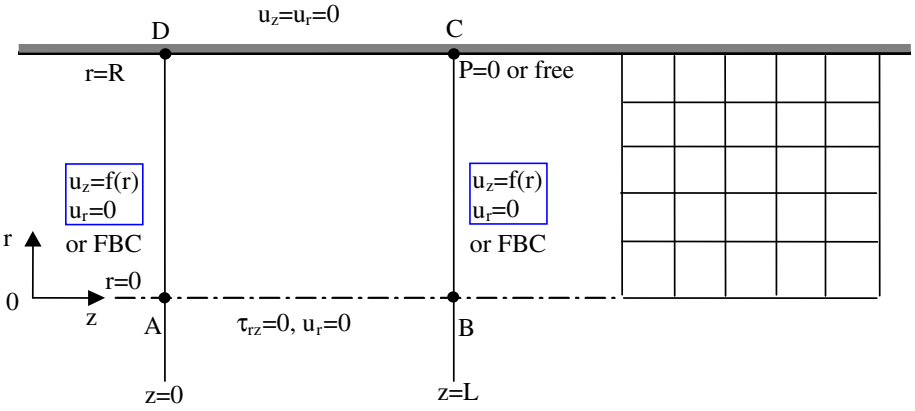


**Fig. 2.** Poiseuille flow in a tube. Boundary conditions and finite element grid (5 × 5). FBC stands for the free boundary condition. Note that for viscoelastic flows each quadrilateral element is split into two triangular elements.

**Table 1**
Finite element mesh characteristics used in the two test axisymmetric problems.

| Mesh | No. of elements (quadrilaterals) | No. of nodes | No. of dof | No. of $\nabla\bar{u}$ dof[a] | No. of $\bar{\bar{\tau}}_{el}$ dof[b] |
|---|---|---|---|---|---|
| Test #1 (Newt.) | 25 | 121 | 602 | – | – |
| Test #1 (PTT) | 200 | 861 | 4032 | 1155 | 924 |
| Test #2 (PTT) | 400 | 1701 | 7912 | 2255 | 1804 |
| Test #2 (Cross) | 1440 | 5973 | 19103 | – | – |

[a] The velocity gradient tensor has five components $\nabla\bar{u} = (\frac{\partial u_z}{\partial z}, \frac{\partial u_z}{\partial r}, \frac{\partial u_r}{\partial z}, \frac{\partial u_r}{\partial r}, \frac{u_r}{r})$.
[b] The stress tensor has four components $\bar{\bar{\tau}} = (\tau_{zz}, \tau_{rr}, \tau_{rz}, \tau_{\theta\theta})$.

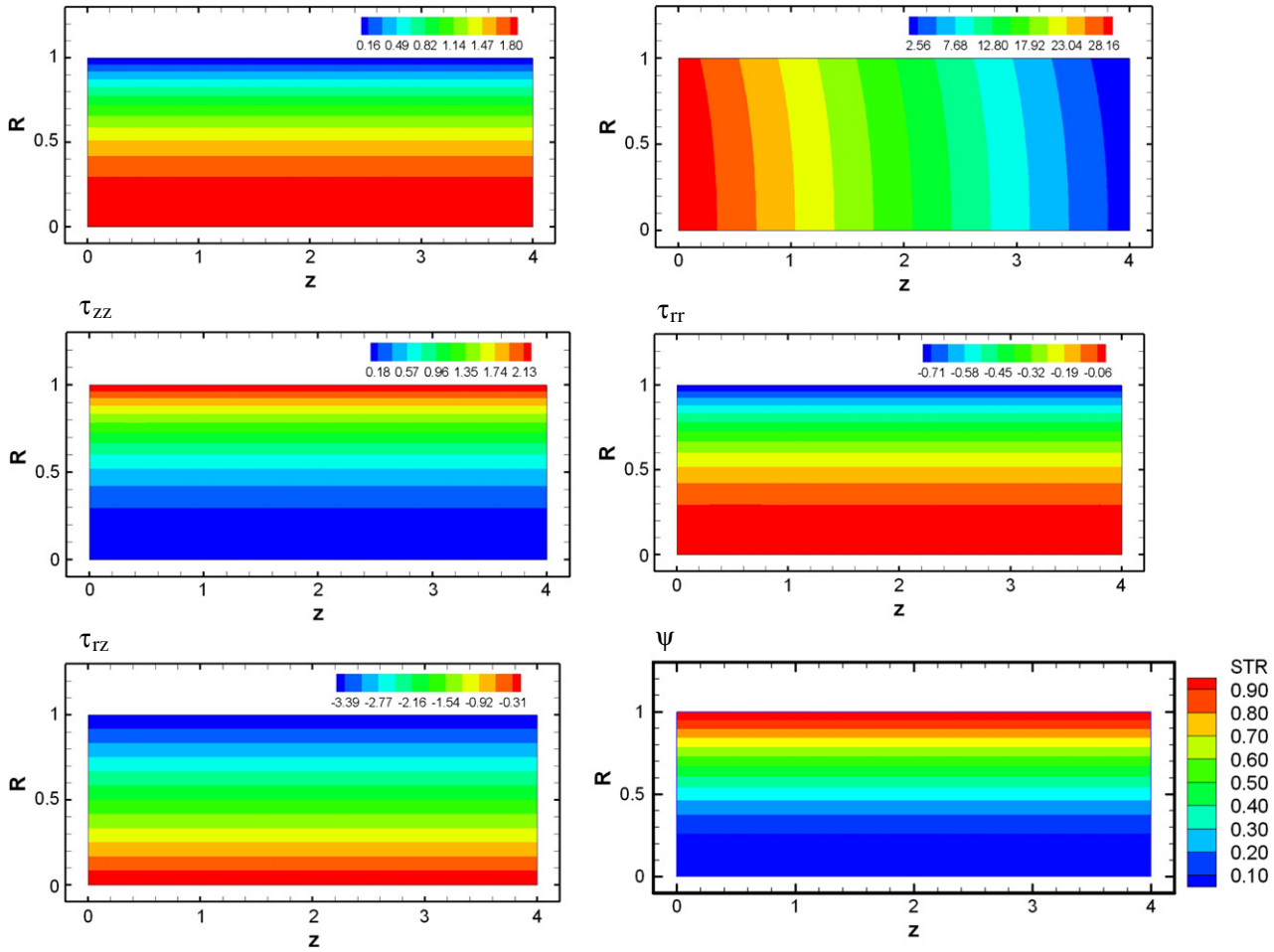


**Fig. 3.** Contours of field variables in Poiseuille flow of a Maxwell fluid (Phan–Thien/Tanner model with $\varepsilon = 0$, $\beta = 0$, $\xi = 0.5$) at $Ws = 0.1$: (a) axial velocity $u_z$, (b) isobars $P$, (c) axial stress $\tau_{zz}$, (d) radial stress $\tau_{rr}$, (e) shear stress $\tau_{rz}$, (f) streamlines. Results by applying the FBC at inflow and outflow boundaries.

$$\nabla^2\psi = -\omega, \tag{8}$$

where $\omega = \frac{\partial u_x}{\partial y} - \frac{\partial u_y}{\partial x}$ is the vorticity in a 2-D planar domain or $\omega = \frac{\partial u_z}{\partial r} - \frac{\partial u_r}{\partial z}$ in an axisymmetric domain.

### 2.2. Rheological models

The relation between stresses and velocity gradients is called the constitutive equation or rheological equation of state. Different fluids obey different constitutive laws.

*Purely viscous fluids* obey the generalized Newtonian fluid model according to:

$$\bar{\bar{\tau}} = \eta(\dot{\gamma})\bar{\bar{\dot{\gamma}}}, \tag{9}$$

where $\bar{\bar{\dot{\gamma}}} = \nabla\bar{u} + \nabla\bar{u}^T$ is the rate-of-strain tensor and $\eta(\dot{\gamma})$ is the apparent viscosity, which is a function of the magnitude $\dot{\gamma}$ of the rate-of-strain tensor given by

$$\dot{\gamma} = \sqrt{\frac{1}{2}II_{\dot{\gamma}}} = \sqrt{\frac{1}{2}(\dot{\gamma} : \dot{\gamma})} \tag{10}$$

where $II_{\dot{\gamma}}$ is the second invariant of the rate-of-strain tensor.

The apparent viscosity is given in its simplest form by the power-law model [23,24]

$$\eta(\dot{\gamma}) = K\dot{\gamma}^{n-1} \tag{11}$$

where $K$ is the consistency index and $n$ is the power-law index (usually $0 < n < 1$, representing a degree of shear-thinning). Another popular model for viscosity computations–among others–is the Cross model [23,24] given by

$$\eta = \frac{\eta_0}{1 + (\lambda_C\dot{\gamma})^{1-n}}. \tag{12}$$

In the above, $\eta_0$ is the zero-shear-rate viscosity, $\lambda_C$ is a characteristic time, and $n$ is again the power-law index. Similar to the Cross model is the Carreau–Yasuda model used in [22].

The effect of temperature on the viscosity is of primordial importance in polymer processing, where tight control of temperatures is required for a successful operation. The viscosity as a

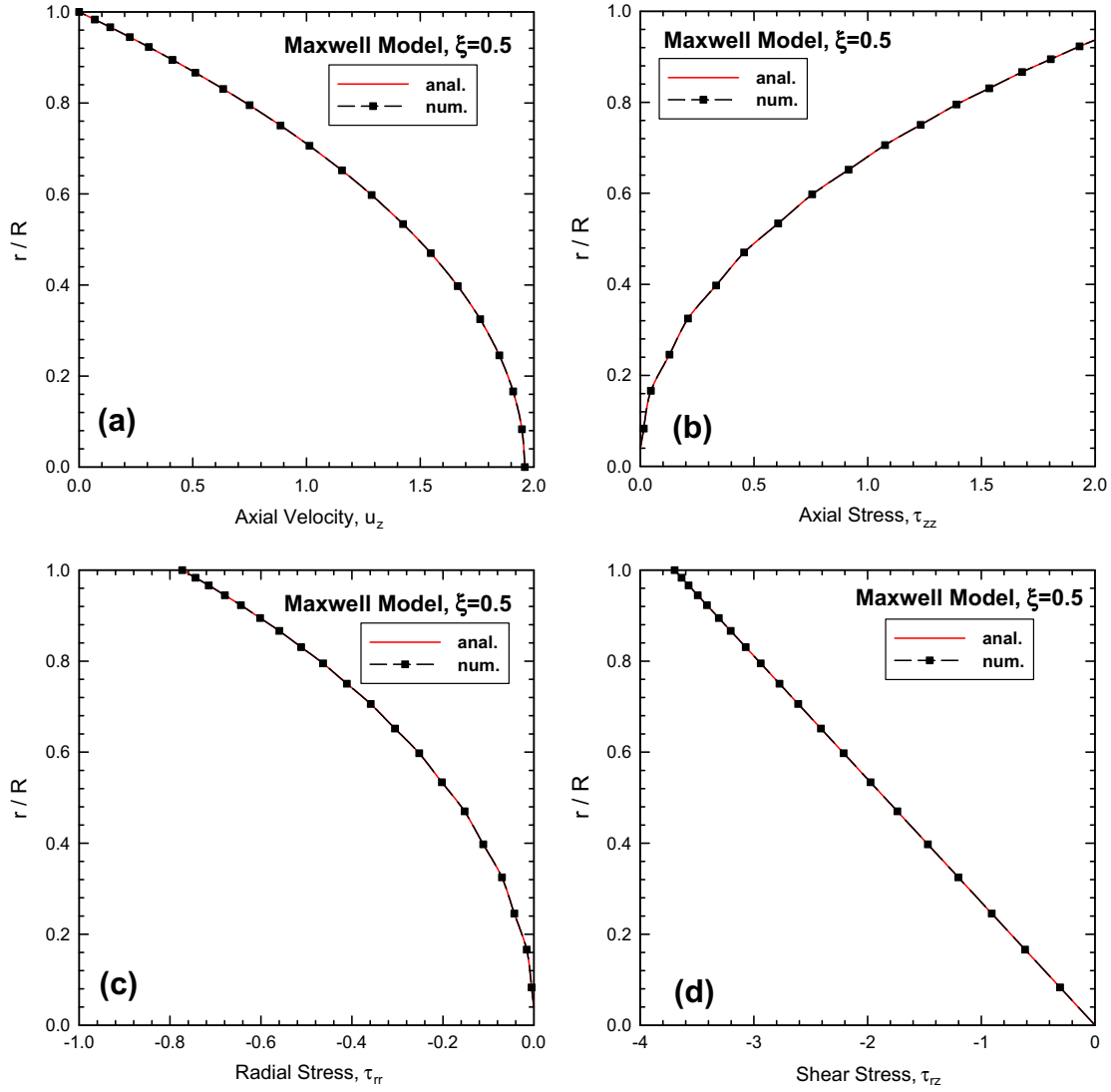


**Fig. 4.** Radial distributions of a Maxwell fluid (Phan–Thien/Tanner model with $\varepsilon = 0$, $\beta = 0$, $\xi = 0.5$) at $Ws = 0.1$: (a) axial velocity $u_z$, (b) axial stress $\tau_{zz}$, (c) radial stress $\tau_{rr}$, (d) shear stress $\tau_{rz}$. Results by applying the FBC at inflow and outflow boundaries. Solid lines are analytical results and symbols are numerical results.

function of temperature is given by an exponential Arrhenius relationship, according to [23,24]

$$\eta_T = \eta_0 a_T = \eta_0 \exp\left[\frac{E_a}{R_g}\left(\frac{1}{T} - \frac{1}{T_0}\right)\right], \tag{13}$$

where $\eta_0$ is the viscosity at a reference temperature, $T_0$, $a_T$ is a temperature-shift factor, $R_g$ is the ideal-gas constant, $E_a$ is the activation energy, $T$ is the absolute temperature in K, and $T_0$ is the absolute reference temperature in K.

*Viscoplastic models* have the addition of a yield stress, below which the material behaves like a solid. The popular viscoplastic models are the Bingham and the Herschel–Bulkley models. A modification of the latter due to Papanastasiou [25] is written as

$$\bar{\bar{\tau}} = \eta\bar{\bar{\dot{\gamma}}} = \left(K\dot{\gamma}^{n-1} + \frac{\tau_y}{\dot{\gamma}}[1 - \exp(-m\dot{\gamma})]\right)\bar{\bar{\dot{\gamma}}}, \text{ for all } \dot{\gamma}, \tag{14}$$

where $\tau_y$ is the yield stress and $m$ is a stress growth exponent that makes the model continuous for all strain rates.

*Viscoelastic models* take into account the elasticity of some fluids (e.g., polymer solutions and melts) and are very complicated functions of the stress and rate-of-strain tensors [23,24]. From a plethora of viscoelastic models, the more widely used in simulations are the upper-convected Maxwell (UCM) model, the Oldroyd-B model, and the Phan–Thien/Tanner (PTT) model. In the latter, there is a splitting of the stress tensor into a purely viscous and a viscoelastic part according to:

$$\bar{\bar{\tau}} = \beta\bar{\bar{\dot{\gamma}}} + \bar{\bar{\tau}}_p, \tag{15}$$

where $\bar{\bar{\tau}}_p$ is the polymeric viscoelastic stress tensor written as follows:

$$Y(\bar{\bar{\tau}}_p)\bar{\bar{\tau}}_p + \lambda\overset{\square}{\bar{\bar{\tau}}}_p = (1-\beta)\bar{\bar{\dot{\gamma}}}, \tag{16}$$

where the symbol $\square$ over the viscoelastic stress tensor denotes the Gordon–Schowalter derivative defined as

$$\overset{\square}{\bar{\bar{X}}} = \frac{D\bar{\bar{X}}}{Dt} - \left\{\nabla\bar{u} - \xi\bar{\bar{\dot{\gamma}}}\right\}^T \cdot \bar{\bar{X}} - \bar{\bar{X}} \cdot \{\nabla\bar{u} - \xi\bar{\bar{\dot{\gamma}}}\}, \tag{17}$$

in which $\bar{\bar{X}}$ is any second-order tensor. In the above the function $Y(\bar{\bar{\tau}}_p)$ may take the linear form

$$Y(\bar{\bar{\tau}}_p) = 1 + \frac{\varepsilon}{1-\beta}\lambda tr(\bar{\bar{\tau}}_p), \tag{18}$$

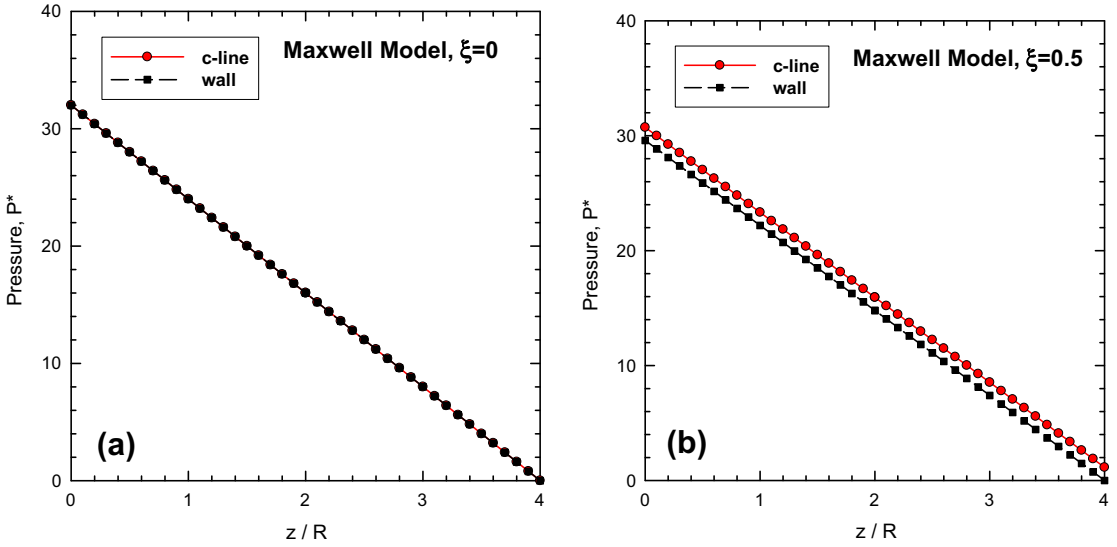


**Fig. 5.** Axial pressure distribution of a Maxwell fluid (Phan–Thien/Tanner model with $\varepsilon = 0$, $\beta = 0$) at $Ws = 0.1$: (a) $\xi = 0$, (b) $\xi = 0.5$.

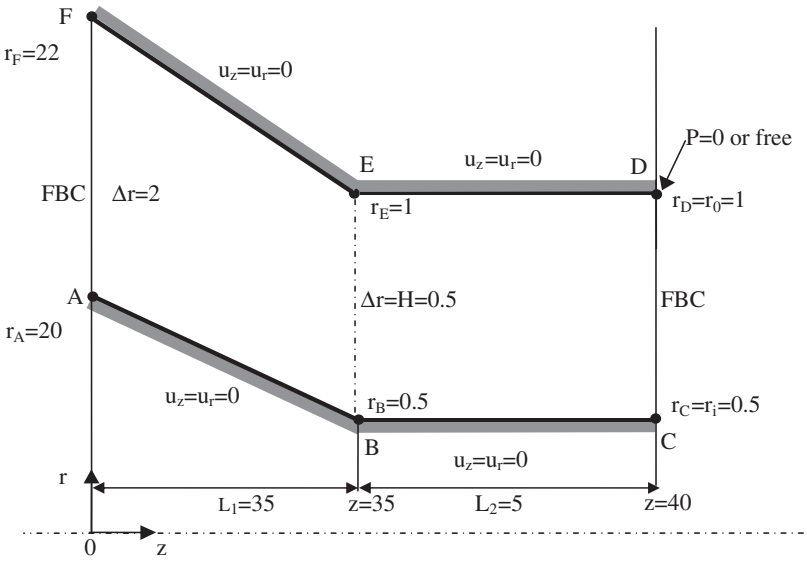


**Fig. 6.** Pressure-driven flow through a tapered annular die. Boundary conditions at the inflow and outflow are the free boundary condition (FBC).

where $\beta$, $\varepsilon$, and $\xi$ are material parameters and $\lambda$ is the relaxation time. When $\varepsilon = 0$ and $\xi = 0$, the PTT model reduces to the Oldroyd-B model. Furthermore, when $\beta = 0$, the PTT reduces to the UCM model.

### 2.3. Dimensionless numbers

The relevant dimensionless numbers of the Navier–Stokes equations need a characteristic length and a characteristic velocity. In the present case, these are the tube radius, $R$, and the average velocity, $U$, at the outflow boundary, respectively. All lengths are made dimensionless by $R$, all velocities by $U$.

The pressures and stresses are scaled with $\mu U/R$. The density is scaled with a reference density $\rho_0$ and the viscosity with a reference viscosity $\mu_0$. Henceforth $\bar{u}$, $p$, $\bar{\bar{\gamma}}$, $\bar{\bar{\tau}}$, $\bar{\bar{\tau}}_p$ will denote dimensionless variables. The following dimensionless numbers are then defined as:

(1) The Reynolds number, $Re$, is a measure of inertia over viscous forces:

$$Re = \frac{\rho U R}{\mu}. \tag{19}$$

For creeping flows, such as those examined in the present work, $Re \approx 0$. However, the case of high $Re$ numbers with the FBC has been investigated in [13] for outflow problems and in [22] with inflow problems.

(2) The Stokes number, $St$, is a measure of gravity over viscous forces:

$$St = \frac{\rho g R^2}{\mu U}. \tag{20}$$

In our previous work [13] we have shown that for some gravity flows (e.g. extrudate swell flows), the FBC is not valid. In the examples examined in the present work, $St = 0$.

(3) The compressibility coefficient, $B_c$, is a measure of fluid compressibility:

$$B_c = \frac{\beta_c \mu U}{R}. \tag{21}$$

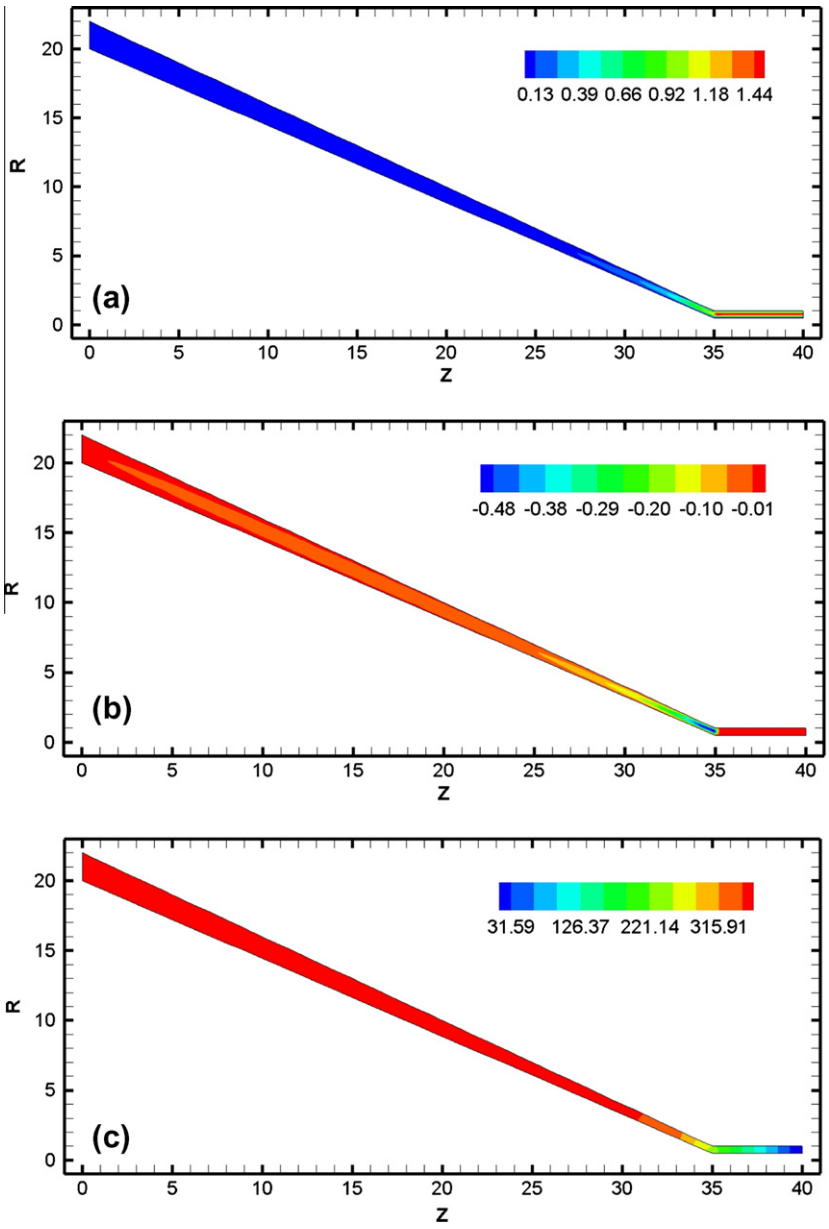


**Fig. 7.** Pressure-driven flow of a Newtonian fluid with an outflow average velocity $u_{z,m} = 1$ through a tapered annular die: (a) $u_z$-contours, (b) $u_r$-contours, (c) isobars $P$. Results by applying the FBC at inflow and outflow boundaries.

For most non-Newtonian fluids, compressibility is very weak and thus neglected, $B_c = 0$. In the present work, an example with weak compressibility has been included.

(4) The pressure-shift coefficient, $B_p$, is a measure of pressure-dependence of the fluid viscosity:

$$B_p = \frac{\beta_p \mu U}{R}. \tag{22}$$

For most non-Newtonian fluids, a pressure-dependence of viscosity is very weak and can be safely neglected, $B_p = 0$. In the present work, an example with a nonzero $B_p$ has been included.

(5) The slip coefficient, $B_{sl}$, is a measure of fluid slip at the wall:

$$B_{sl} = \frac{\beta_{sl} \mu}{R}. \tag{23}$$

For some non-Newtonian fluids, slip can be strong and should be included. In the present work, an example with strong slip has been included.

(6) The Peclet number, $Pe$, is a measure of fluid thermal convection over diffusion:

$$Pe = \frac{\rho c_p U R}{k}. \tag{24}$$

In some non-Newtonian fluids processing, thermal convection can be very strong with a Peclet number in the thousands. In the present work, an example with $Pe = O(10^{+3})$ has been included.

(7) The Nahme–Griffith number, $Na$, is a measure of fluid viscous dissipation over diffusion:

$$Na = \frac{\bar{\eta} E_a U^2}{k R_g T_0^2}, \tag{25}$$

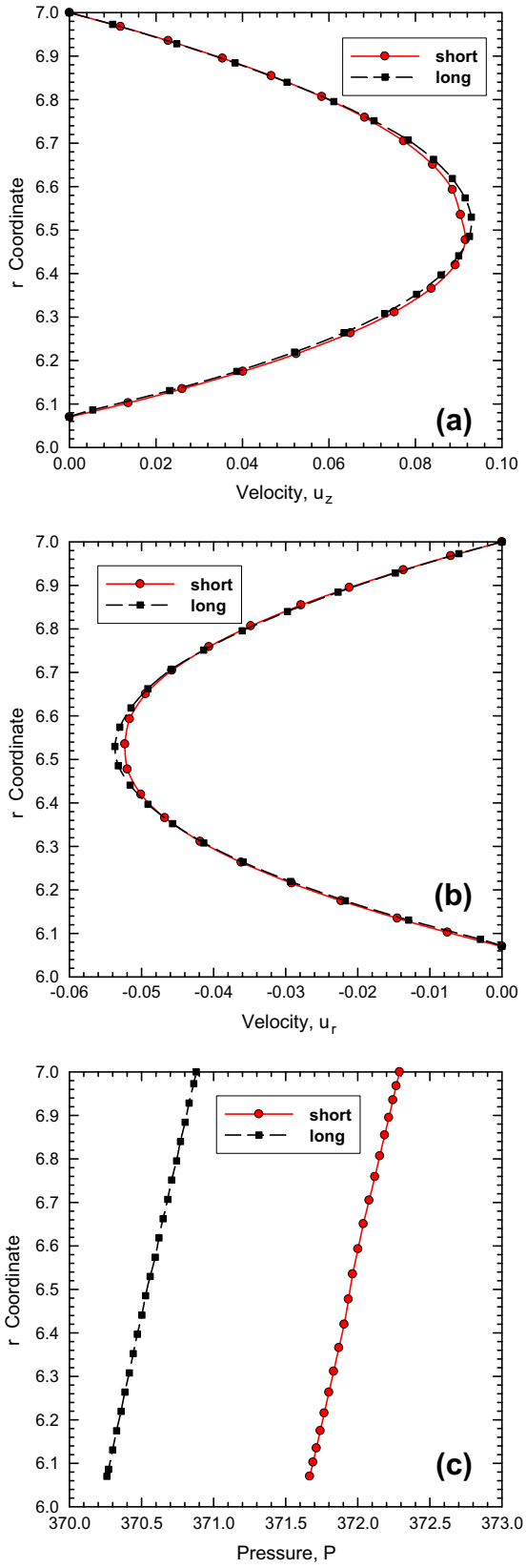


**Fig. 8.** Radial profiles of a Newtonian fluid with an outflow average velocity $U = 1$ through a tapered annular die: (a) $u_z$-velocity, (b) $u_r$-velocity, (c) pressure. Results shown at $z = 25$ by applying the FBC at inflow either for the full domain (long) or the truncated domain starting at $z = 25$ (short).

where $\bar{\eta} = f(U/R)$ is a nominal viscosity given by the constitutive model (Eq. (9)) at a nominal shear rate of $U/R$. In some non-Newtonian fluids processing, viscous dissipation can be strong with a Nahme number greater than 1. In the present work, an example with $Na = O(10)$ has been included.

(8) The Weissenberg number, $Ws$, is a measure of fluid viscoelasticity defined by:

$$Ws = \lambda \dot{\gamma}_A = \lambda \frac{U}{R}, \tag{26}$$

where $\lambda$ is the relaxation time of the fluid, $\dot{\gamma}_A$ is the apparent shear rate ($=U/R$). For the Newtonian or purely viscous fluids, $Ws = 0$. For non-Newtonian viscoelastic fluids, $Ws > 0$, and such examples are included in the present work.

## 3. Method of solution

The numerical solution is obtained with the Finite Element Method (FEM), using two different programs. The first (called *uvpth*) employs as primary variables the two velocities, pressure, temperature and free surface location (*u–v–p–T–h formulation*) and uses a Picard (P) or direct substitution iterative scheme [26]. The second program is a viscoelastic code which employs as primary variables, apart from the velocities and the pressure, the stresses and the velocity gradients, and uses the Newton–Raphson (N–R) iterative scheme [12,27]. The *uvpth* code has been developed and used mainly for non-Newtonian (pseudoplastic and viscoplastic) problems, for which it has been found more suitable. In the present work, both programs were modified to account for implementing the FBC at the inlet.

The major features of the *uvpth* code are as follows. The physical domain is discretized using quadrilateral elements. The velocity vector, the temperature, and the stream function are approximated with 9-node Lagrangian basis functions, $\phi^i$, and the pressure is approximated with 4-node Lagrangian basis functions, $\psi^i$.

For the governing conservation Eqs. (1)–(3) and the stream function (Eq. (8)), the finite element/Galerkin method is employed, which after applying the divergence theorem results in the following weak forms:

$$\int_\Omega \nabla \cdot \bar{u}\psi^i d\Omega = 0, \tag{27}$$

$$\int_\Omega [(Re\bar{u} \cdot \nabla \bar{u})\phi^i + (-p\bar{\bar{I}} + \bar{\bar{\tau}}) \cdot \nabla \phi^i] d\Omega = \int_\Gamma \bar{n} \cdot (-p\bar{\bar{I}} + \bar{\bar{\tau}})\phi^i d\Gamma, \tag{28}$$

$$\int_\Omega [(Pe\bar{u} \cdot \nabla T)\phi^i + \nabla T \cdot \nabla \phi^i - (\bar{\bar{\tau}} : \nabla \bar{u})\phi^i] d\Omega = \int_\Gamma (\bar{n} \cdot \nabla T)\phi^i d\Gamma, \tag{29}$$

$$\int_\Omega (-\nabla \psi \nabla \phi^i + \omega \phi^i) d\Omega = \int_\Gamma (\bar{n} \cdot \nabla \psi)\phi^i d\Gamma. \tag{30}$$

where $d\Omega$ and $d\Gamma$ are the differential volume and surface area, respectively. In the above, the right-hand side (RHS) of Eqs. (28)–(30) constitute the free (open) boundary conditions to be applied at the outflow as well as the inflow boundaries. These terms are not necessarily zero there and must be evaluated at each iteration. All necessary information about the discrete formulation implemented in the *uvpth* program has been given in detail before [13,28,29] and will not be repeated here.

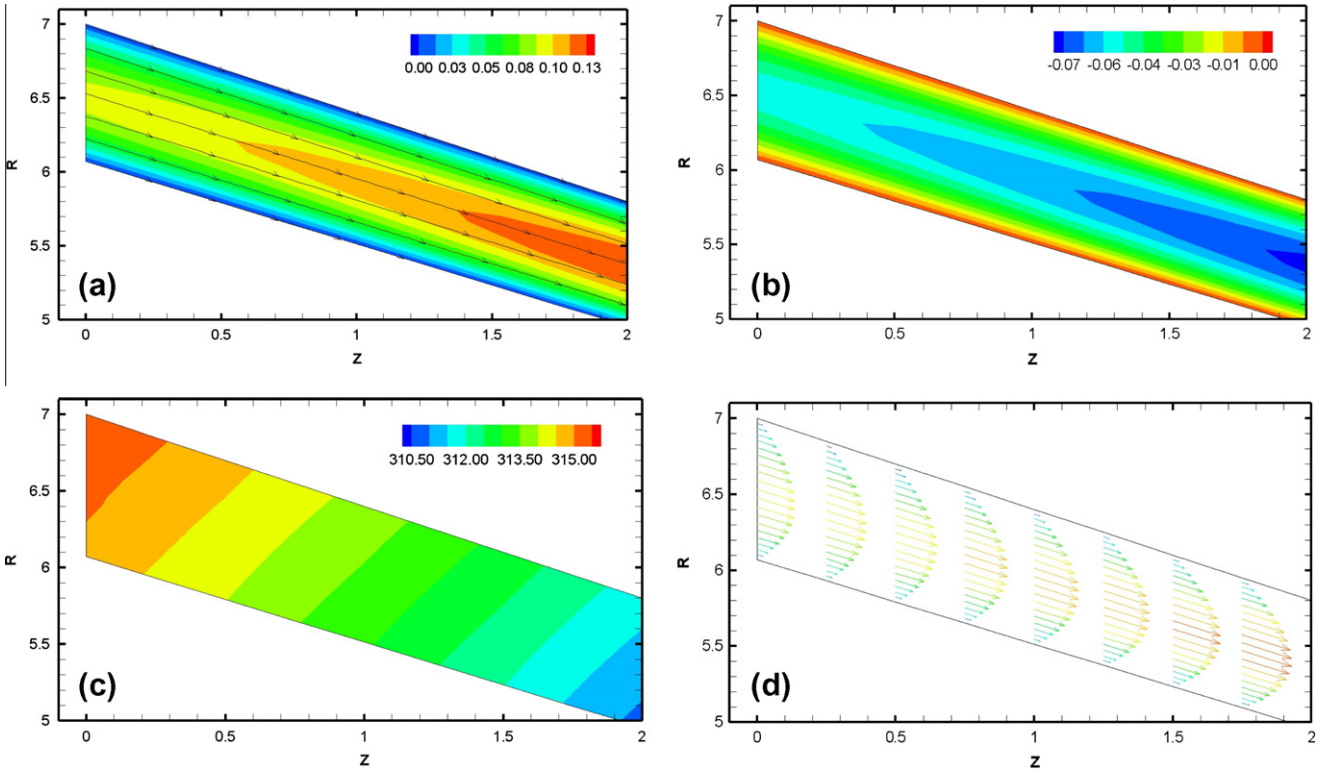


**Fig. 9.** Pressure-driven flow of a Phan–Thien/Tanner fluid ($\varepsilon = 0.05$, $\beta = 0$, $\xi = 0.1$) at $Ws$=0.1 through a tapered annular die: (a) $u_z$-contours and streamlines, (b) $u_r$-contours, (c) isobars $P$, (d) velocity vectors. Results near the inlet of the truncated domain (short) at $z = 25$ by applying the FBC at inflow and outflow boundaries.

### 3.1. Finite element formulation for differential viscoelastic models

Regarding the second program for viscoelastic flows governed by differential models of the PTT type [12,27], its major features are as follows. The physical domain is discretized using triangular elements, which may be produced by subdivision of a 9-node quadrilateral element into two triangular ones. The velocity vector is approximated with 6-node Lagrangian basis functions, $\phi^i$, and the pressure, the elastic stresses as well as the velocity gradients with 3-node Lagrangian basis functions, $\psi^i$.

For the mass balance, Eq. (27) remains the same. For the momentum balance, the finite element/Galerkin method, after applying the divergence theorem, results in the following weak form:

$$\int_\Omega [Re\bar{u}\cdot\nabla\bar{u}\phi^i - p\nabla\phi^i + \nabla\phi^i\cdot\bar{\bar{\tau}}_{el} + \nabla\phi^i\cdot\bar{\bar{\dot{\gamma}}}]d\Omega = \int_\Gamma [\bar{n}\cdot(-p\bar{\bar{I}} + \bar{\bar{\tau}})]\phi^i d\Gamma. \quad (31)$$

The surface integral that appears in the momentum equation is split into several parts, each one corresponding to a boundary of the physical domain, and the relevant boundary condition is applied therein.

In order to solve accurately and efficiently the viscoelastic PTT model, the Elastic-Viscous Split Stress (EVSS) formulation is employed [30]. This method consists of splitting the polymeric part of the extra stress tensor into a purely elastic and a viscous part

$$\bar{\bar{\tau}}_p = \bar{\bar{\tau}}_{el} + (1-\beta)\bar{\bar{\dot{\gamma}}}. \quad (32)$$

The success of this scheme resides in the fact that the elliptic nature of the momentum equations is ensured even for $\beta = 0$. Brown et al. [31] proposed a modification of this model (EVSS-G) according to which an independent interpolation of the components of the velocity gradient tensor is introduced in order to satisfy the compatibility in the approximation between elastic stress and velocity gradients in the constitutive equation. The corresponding equation that must be solved is

$$\int_\Omega (\bar{\bar{G}} - \nabla\bar{u})\psi^i d\Omega = 0. \quad (33)$$

Finally, the constitutive equation for the PTT model, due to its hyperbolic character, is discretized using the SUPG method proposed by Brooks and Hughes [32]

$$\int_\Omega \left[ Y(\bar{\bar{\tau}}_p)\bar{\bar{\tau}}_{el} + Ws\overset{\square}{\bar{\bar{\tau}}}_{el} + Ws(1-\beta)\left(\overset{\square}{\bar{\bar{G}}} + \overset{\square}{\bar{\bar{G}}}^T\right) - (1-\beta)(1-Y(\bar{\bar{\tau}}_p))\left(\overset{\square}{\bar{\bar{G}}} + \overset{\square}{\bar{\bar{G}}}^T\right)\right] w^i d\Omega = 0. \quad (34)$$

The new weighting function $w^i$ is formed from the finite element basis function for the elastic stress components as

$$w^i = \psi^i + \frac{h}{|u_m|}\bar{u}\cdot\nabla\psi^i, \quad (35)$$

where $|u_m|$ is the magnitude of the mean velocity and $h$ is a characteristic length at the particular element. The mean velocity $|u_m|$ in an element is defined as $|u_m| = \frac{1}{3}\sum_{n=1}^{3}|u|_n$, with $|u|_n$ denoting the magnitude of the velocity at the vertices of the corresponding triangular element. As a characteristic length, $h$, we used the square root of the area of each triangular element.

### 3.2. Boundary conditions

Along the walls and in cases where there is no slip, we impose the usual no-slip, no-penetration conditions

$$u_r = 0, \quad u_z = 0. \quad (36a)$$

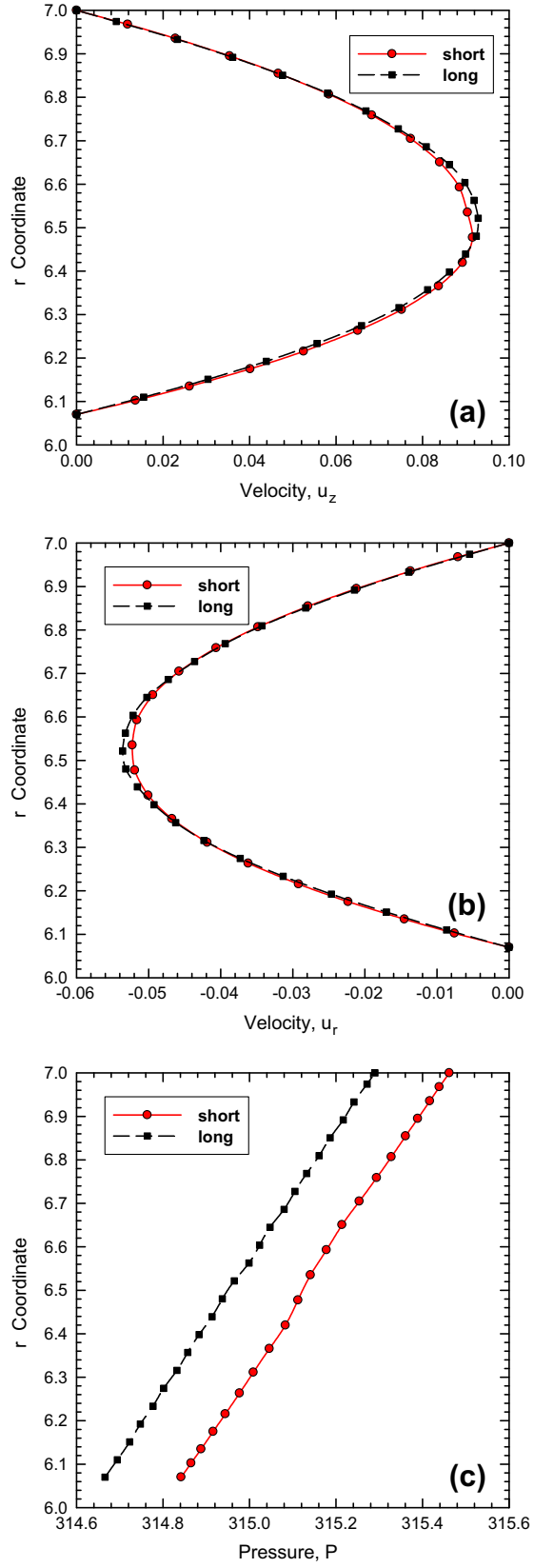


**Fig. 10.** Radial profiles of a Phan–Thien/Tanner fluid ($\varepsilon = 0.05$, $\beta = 0$, $\xi = 0.1$) at $Ws = 0.1$ through a tapered annular die: (a) $u_z$-velocity, (b) $u_r$-velocity, (c) pressure. Results shown at $z = 25$ by applying the FBC at inflow either for the full domain (long) or the truncated domain starting at $z = 25$ (short).

In the case of slip at the wall, these become:

$$\bar{n}\cdot\bar{u}=0,\quad \bar{t}\cdot\bar{u}=B_{sl}(\bar{t}\bar{n}:\bar{\bar{\tau}}). \tag{36b}$$

Also the stream function is set to 0 at one wall and equal to the flow rate at the other wall.

At the outflow boundary we apply the FBC [1] by evaluating the relevant term of the RHS of Eq. (27) as follows (for axisymmetric geometries)

$$\int_\Gamma(\bar{n}\cdot(-p\bar{\bar{I}}+\bar{\bar{\tau}}))\varphi^i d\Gamma=\underbrace{\int_{\Gamma_{FBC}}\begin{pmatrix}n_r(-p+\tau_{rr})+n_z\tau_{rz}\\ n_r\tau_{rz}+n_z(-p+\tau_{zz})\end{pmatrix}\varphi^i d\Gamma}_{\text{free boundary condition}}, \tag{37}$$

$$\int_\Gamma(\bar{n}\cdot\nabla T)\phi^i d\Gamma=\underbrace{\int_{\Gamma_{FBC}}\left(n_r\frac{\partial T}{\partial r}+n_z\frac{\partial T}{\partial z}\right)\varphi^i d\Gamma}_{\text{free boundary condition}}, \tag{38}$$

$$\int_\Gamma(\bar{n}\cdot\nabla\psi)\phi^i d\Gamma=\underbrace{\int_{\Gamma_{FBC}}\left(n_r\frac{\partial\psi}{\partial r}+n_z\frac{\partial\psi}{\partial z}\right)\varphi^i d\Gamma}_{\text{free boundary condition}}. \tag{39}$$

So far, this is a standard procedure, and similar schemes have been widely used in the literature [1–12] mainly for the momentum Eq. (37).

The novelty introduced in this paper is how we treat the boundary conditions at the inflow boundary. In most cases found in the literature, a fully developed velocity profile is assumed far upstream that corresponds to the fluid model at hand, and an analytical model is derived or a 1D numerical solution is imposed. Such an assumption, however, is not always possible or there may be situations that a numerical solution is difficult to implement. This kind of situation makes the idea of the FBC at the inflow boundary very appealing.

At the inflow boundary (see Fig. 1), the relevant terms of the RHS of Eqs. (28)–(30) are evaluated in the same way as at the outflow boundary, i.e., using Eqs. (37)–(39). No further information is needed and no other boundary condition has to be explicitly imposed! The problem is closed by demanding that the dimensionless mean velocity at the outflow boundary, $u_{z,m}$, is equal to unity, since the mean velocity at the outflow boundary, $U$, is used as a characteristic velocity for non-dimensionalizing the governing equations. Therefore the additional equation that arises is

$$u_{z,m}=\frac{\int_{r_i}^{r_o}u_z r dr}{\int_{r_i}^{r_o}r dr}=1, \tag{40}$$

where $r_o$ is the outer radius and $r_i$ is the inner radius. In its discrete form this is written as:

$$\frac{2}{r_o^2-r_i^2}\left[\sum_{i=1}^{E}\sum_{j=1}^{G}\left[\left(\sum_{k=1}^{N}u_i^k r_i^k\phi^k\right)\right]w^j\right]=1, \tag{41}$$

where $E$is the number of elements along the inflow, $G$ the number of Gaussian points for each element along the inflow side (=3), $N$ is the number of nodes for each element belonging to the inflow side (=3), $u_i^k$ are the nodal values of the velocity, and $w^j$ are the Gaussian weights.

The reason why Eq. (40) is necessary can be easily understood by considering the classical problem of 1D Poiseuille flow. In this simple problem one imposes the boundary conditions at both ends, and in addition we have to set some flow rate (or equivalently the mean velocity) in order to evaluate the pressure drop or the maximum velocity.

Dimakopoulos et al. [22] replaced the continuity at one end of the inflow boundary (e.g. the upper wall) with Eq. (40) and then used this equation, instead of the continuity, to compute the

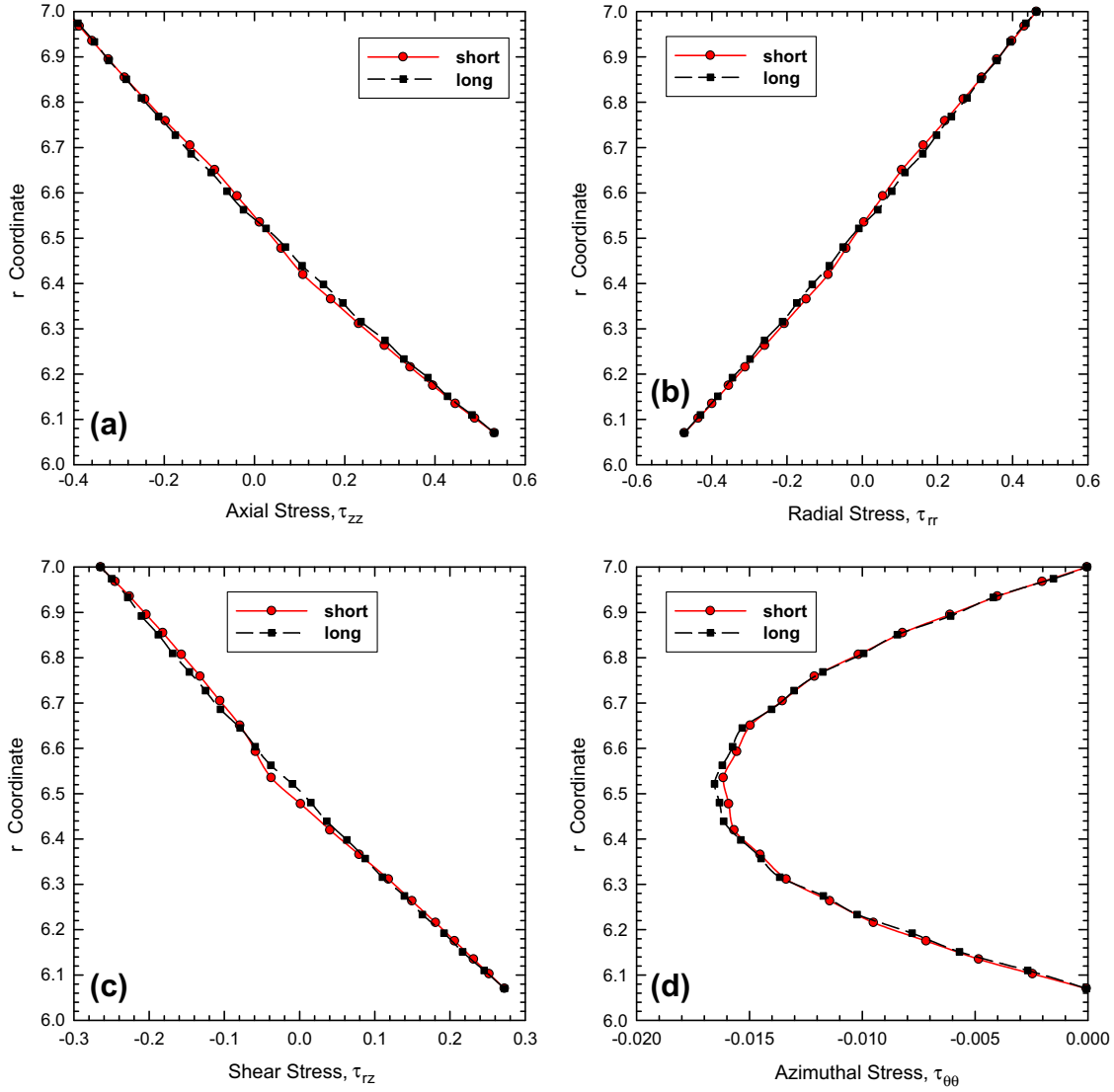


**Fig. 11.** Radial stress profiles of a Phan–Thien/Tanner fluid ($\varepsilon = 0.05$, $\beta = 0$, $\xi = 0.1$) at $Ws = 0.1$ through a tapered annular die: (a) axial $\tau_{zz}$-stress, (b) radial $\tau_{rr}$-stress, (c) shear $\tau_{rz}$-stress, (d) azimuthal $\tau_{\theta\theta}$-stress. Results shown at $z = 25$ by applying the FBC at inflow either for the full domain (long) or the truncated domain starting at $z = 25$ (short).

**Table 2**
Values of the various material data for the FEP melt at 371°C [35].

| Parameter | Value |
|---|---|
| $\beta_c$ | 0.00095 $MPa^{-1}$ |
| $\beta_p$ | 0.03 $MPa^{-1}$ |
| $m$ | $1.39 \times 10^{-4}$ $Pa^{n_p-1}$ |
| $n_p$ | 0.54 |
| $\beta_{sl}$ | 400 cm/(s $MPa^b$) |
| $b$ | 2.0 |
| $\rho$ | 1.492 g/$cm^3$ |
| $c_p$ | 0.96 J/(g K) |
| $k$ | 0.00255 J/(s cm K) |
| $E_a$ | 50,000 J/mol |
| $R_g$ | 8.3143 J/(mol K) |
| $T_0$ | 371 °C (644 K) |

**Table 3**
Parameters for the FEP melt obeying the Cross model (Eq. (11)) at 371 °C [35].

| Parameter | Value |
|---|---|
| $\eta_0$ | 1542.3 Pa s |
| $\lambda_C$ | 0.0049 s |
| $n$ | 0.316 |

pressure at that node. It was shown that the proposed scheme gave very good numerical results without any oscillations or unrealistic velocity and pressure profiles. Although this scheme worked quite well for horizontal pipes with a centerline, we found during trials that this is definitely not the case for more general cases, e.g., an inclined annular pipe. We found that this scheme could result in violating the continuity equation near the wall leading to unphysical solutions. This should come as no surprise since the continuity at the wall node has been removed from our system of equations.

The current approach is somewhat different. Eq. (40) is used to compute the velocity at one point of the inflow boundary, ideally at the position that the maximum velocity is expected to arise or close to it. The reason for choosing a node as close as possible to the position of the maximum velocity is the fact that the value of the velocity in that region will have the biggest impact on the

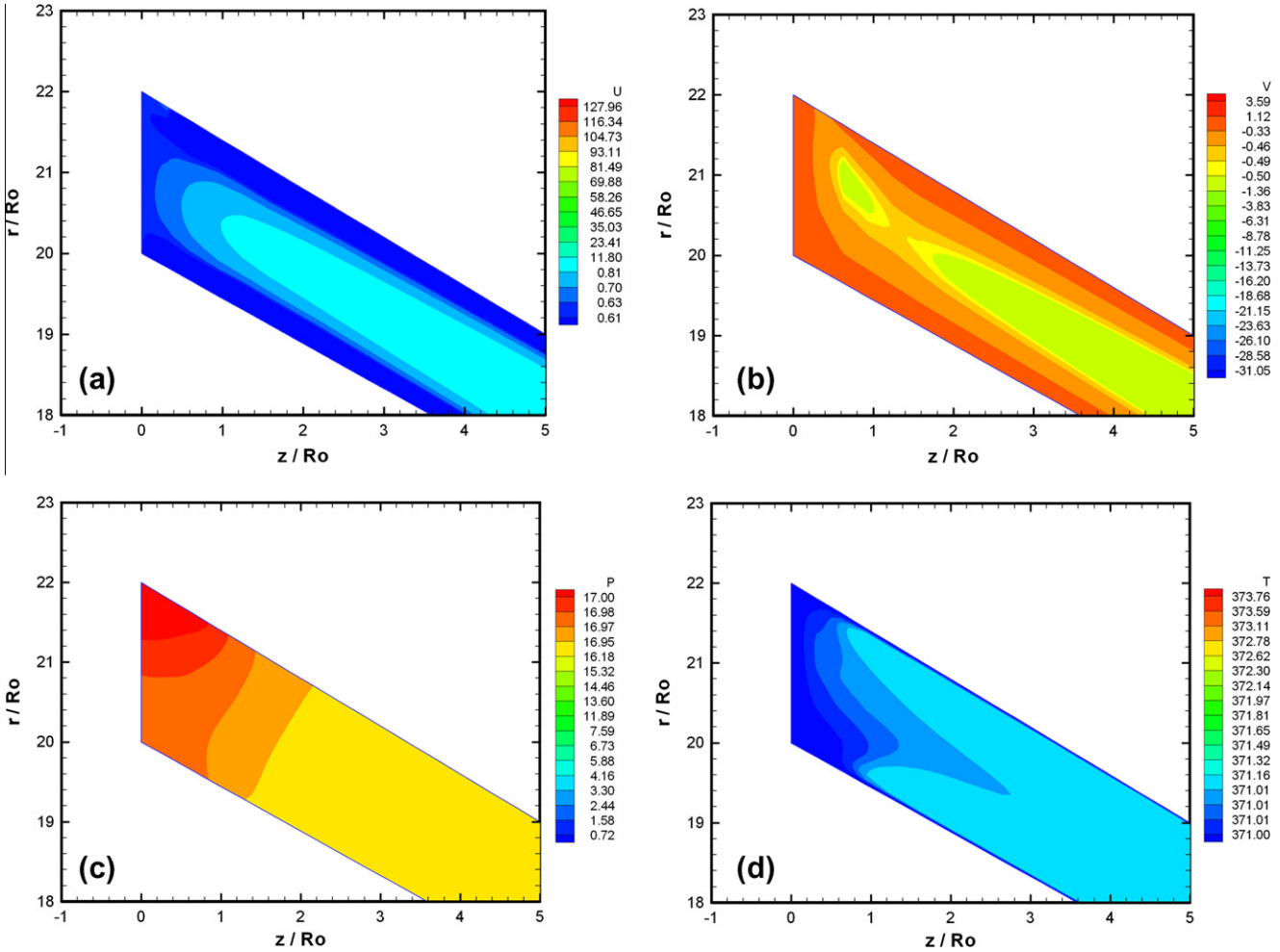


**Fig. 12.** Pressure-driven flow of a FEP melt through a tapered annular die at $\dot{\gamma}_A = 5600\,s^{-1}$ ($Re = 1.89 \times 10^{-3}$, $B_c = 3.57 \times 10^{-4}$, $B_p = 1.13 \times 10^{-2}$, $B_{sl} = 0.821$, $Pe = 2859$, $Na = 10.89$): (a) $u_z$-contours, (b) $u_r$-contours, (c) isobars $P$, (d) isotherms $T$. Results near the inlet by applying as inflow boundary conditions a plug velocity profile and a constant temperature profile. The results are not smooth.

mean velocity. Choosing a node close to the wall would not be wise since we expect that the velocity there will be very small and thus its effect on the mean velocity will be minimal. This suggested scheme is in direct analogy with the 1D Poiseuille flow, where we use the imposition of the mean velocity (Eq. (40)) to evaluate the maximum velocity. As it will be shown below, this scheme works very well in a great variety of problems.

There are more than one ways to implement Eq. (41) in a FEM program. When using the Newton–Raphson iterative scheme, we replace the momentum in the principal (axial) direction of the flow with the residual of Eq. (40) or its discrete form, Eq. (41). The Jacobian entries are evaluated and replace the corresponding line in the Jacobian matrix for that degree of freedom. We also have to set a datum pressure and as such we impose a zero value to the pressure at a node of the outflow boundary.

When using the Picard iterative scheme one usually has to solve the following algebraic system of equations

$$\underline{\underline{S}} \cdot \underline{x} = \underline{F}, \tag{42}$$

where $\underline{\underline{S}}$ is the stiffness matrix, $\underline{x}$ is the vector of the unknown velocities and pressure, and $\underline{F}$ is the load vector. There are two equivalent ways of how to handle Eq. (40). One way is to simply set the residual $F^i$ for the dof at hand ($i$th), which corresponds to the value of the velocity in the principal direction of the flow, equal to

$$F^i = u_{z,m} - 1 - (\underline{\underline{S}} \cdot \underline{x})^i. \tag{43}$$

This way, without making any changes to the stiffness matrix $\underline{\underline{S}}$, we are able to impose $u_{z,m} = 1$ and fix the average velocity. This is the method of choice with integral viscoelastic models, where the elastic stresses all enter the RHS [15]. The other way (much more powerful) is to have contributions in the LHS "stiffness" matrix from the basis functions $\phi^k$ according to Eq. (41) corresponding to the dof at hand, while the RHS "load" vector simply has the set mean velocity equal to 1. The former approach is simpler but it requires many more iterations than the latter approach which converges fast (for linear problems in one iteration). In the second approach the only information needed is the basis (shape) functions of all the inlet finite elements, which are readily available and calculated only once. Also with the Picard scheme we have found that it is important not to set a datum pressure anywhere equal to zero, but after the solution is obtained, to subtract all pressure values from a datum pressure, usually taken as the pressure value of the exit node at the wall.

The criteria for termination of the iterative process were for N–R a norm-of-the-residuals $\|e\| < 10^{-8}$ and for P both the norm-of-the-error and the norm-of-the-residuals $<10^{-4}$. This difference in the stopping criteria reflects the superiority of the quadratic N–R scheme compared with the linear P scheme.

Another feature is the loss of convergence in viscoelastic flows for some high value of the Weissenberg number (also called the HWNP) [33] when using the FBC at inlet. In all cases tested it was found that this does not influence the HWNP limit.

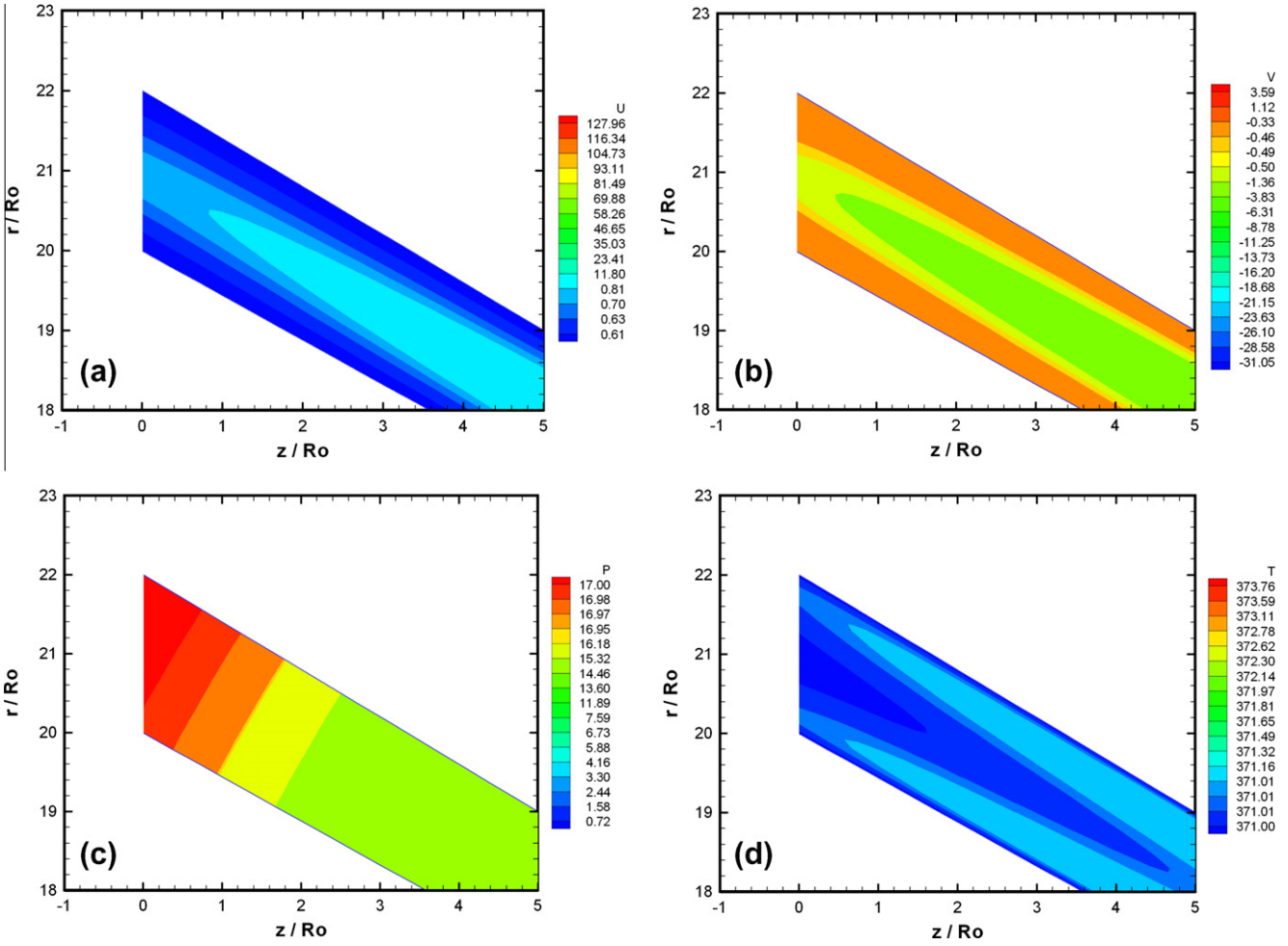


**Fig. 13.** Pressure-driven non-isothermal flow with slip at the wall of a FEP melt through a tapered annular die at $\dot{\gamma}_A = 5600\,s^{-1}$ ($Re = 1.89 \times 10^{-3}$, $B_c = 3.57 \times 10^{-4}$, $B_p = 1.13 \times 10^{-2}$, $B_{sl} = 0.821, Pe = 2859$, $Na = 10.89$): (a) $u_z$-contours, (b) $u_r$-contours, (c) isobars $P$, (d) isotherms $T$. Results near the inlet by applying as inflow boundary condition the FBC. The results are now smooth.

## 4. Results and discussion

### 4.1. Poiseuille flow of a Maxwell fluid (Test #1)

The very first test was done for simple pressure-driven (Poiseuille) flow in a tube or between flat plates for a Newtonian fluid with both codes. Fig. 2 shows the solution domain and boundary conditions, together with a $5 \times 5$ finite element grid in the understanding that if the method is correct it should work even with the sparsest of grids. By assuming both at inlet and outlet the FBC and setting the mean velocity equal to 1 at one inlet node (the centerline $u_z$ dof), the results gave the perfect parabolic velocity profile everywhere and the linear pressure drop according to the well-known analytical solution.

We then tested the implementation of the FBC with the viscoelastic PTT fluid ($\varepsilon = 0$, $\beta = 0$, $\xi = 0.5$) in Poiseuille flow in a tube for further code validation. The choice of parameters is such so that it corresponds to the Maxwell fluid but with a non-zero second normal-stress difference ($\xi = 0.5$). This means that it uses a combination of upper convected (UCM) and lower convected (LCM) derivatives. The value of $\xi = 0.5$ corresponds to a ratio $N_2/N_1 = -\xi/2 = -0.25$. Again the boundary conditions were as shown in Fig. 2. We have used in these calculations a denser grid with mesh characteristics given in Table 1. These include the number of elements (quadrilateral), nodes, degrees of freedom (dof), i.e., $u$–$v$–$p$–$\nabla\bar{u}$–$\bar{\bar{\tau}}$ for the viscoelastic case. Because of axisymmetry only one half of the flow domain is considered. Then there are five velocity-gradient components $\nabla\bar{u} = (\frac{\partial u_z}{\partial z}, \frac{\partial u_z}{\partial r}, \frac{\partial u_r}{\partial z}, \frac{\partial u_r}{\partial r}, \frac{u_r}{r})$ and 4 stress components $\bar{\bar{\tau}} = (\tau_{zz}, \tau_{rr}, \tau_{rz}, \tau_{\theta\theta})$.

The boundary conditions in this type of problem are:

(i) along the inlet DA we either impose a fully-developed velocity profile or the FBC is prescribed for a given flow rate or average velocity $u_{z,m} = 1$;
(ii) along the symmetry line AB, $\tau_{rz} = 0$, $u_r = 0$;
(iii) along the die wall no slip conditions are imposed, $u_z = u_r = 0$;
(iv) along the outlet BC either a fully-developed profile is given (and this is a necessity for viscoelastic fluids due to the presence of non-zero normal stresses), or the FBC is prescribed. The pressure P is set to 0 at point C or is left free when using the FBC [13].

The Maxwell fluid with a non-zero second normal-stress difference ($\xi \neq 0$) is obtained from the PTT model by setting $\varepsilon = 0$ and $\beta = 0$. For this case, Alves et al. [34] presented an analytical solution. In cylindrical coordinates the solution is:

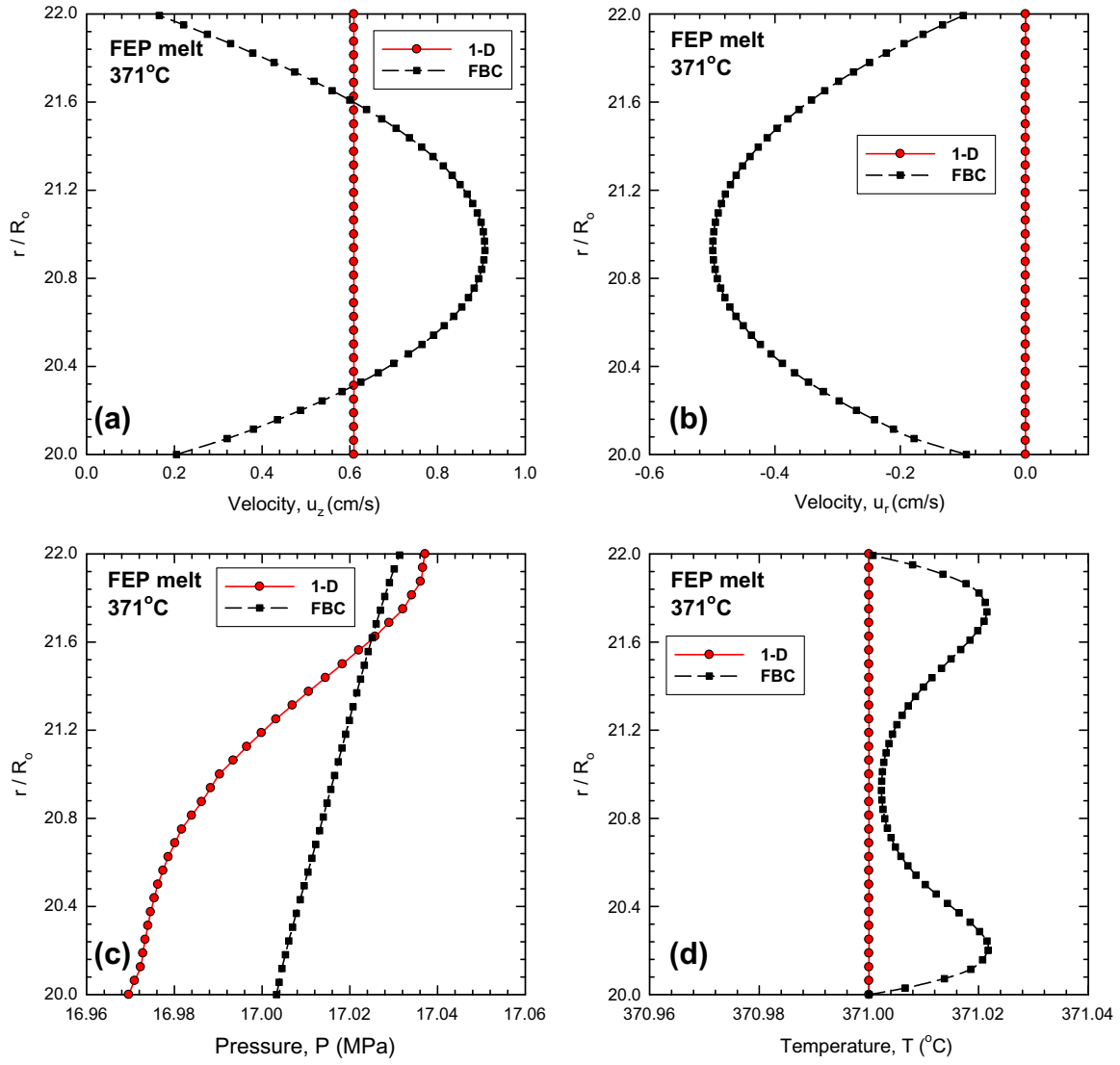


**Fig. 14.** Radial profiles of a FEP melt through a tapered annular die at $\dot{\gamma}_A = 5600\ s^{-1}$ ($Re = 1.89 \times 10^{-3}$, $B_c = 3.57 \times 10^{-4}$, $B_p = 1.13 \times 10^{-2}$, $B_{sl} = 0.821$, $Pe = 2859$, $Na = 10.89$): (a) $u_z$-velocity, (b) $u_r$-velocity, (c) pressure, (d) temperature. Results shown at inlet by applying either the FBC at inflow or a plug velocity profile and constant temperature profile.

$$u_z(r) = -\frac{a\varepsilon(1-r^2)(1-\xi)}{2Ws[\xi(2-\xi)]^{3/2}} - \frac{1}{aWs\sqrt{\xi(2-\xi)}} \left(1+\frac{2\varepsilon(1-\xi)}{\xi(2-\xi)}\right)\left(\ln\frac{1+\sqrt{1-(ar)^2}}{1+\sqrt{1-a^2}} + \sqrt{1-a^2} - \sqrt{1-(ar)^2}\right), \tag{44a}$$

$$\tau_{rr}(r) = -\frac{1-\sqrt{1-(ar)^2}}{8Ws(2-\xi)}, \tag{44b}$$

$$\tau_{rz}(r) = -\frac{ar}{8Ws\sqrt{\xi(2-\xi)}}, \tag{44c}$$

$$\tau_{zz}(r) = \frac{1-\sqrt{1-(ar)^2}}{8Ws\xi}, \tag{44d}$$

$$\frac{N_2}{N_1} = -\frac{\xi}{2}, \tag{44e}$$

where the parameter $a$ is given by

$$\frac{4Ws\sqrt{\xi(2-\xi)}}{a} = \frac{2}{a^2}\left(1+\frac{2\varepsilon(1-\xi)}{\xi(2-\xi)}\right)\left(1-\frac{2}{3}\sqrt{1-a^2}-\frac{2}{3}\frac{1-\sqrt{1-a^2}}{a^2}\right) - \frac{\varepsilon(1-\xi)}{\xi(2-\xi)}. \tag{45}$$

Setting $\varepsilon = 0$, $\xi = 0.5$ and $Ws = 0.1$, we solve numerically Eq. (45) and get $a = 0.6405$. Using this value for $a$ we find: $\tau_{rz}(1) = -3.698$, $\tau_{rr}(1) = -0.773$ and $\tau_{zz}(1) = 2.320$ and $|\tau| = \sqrt{\frac{1}{2}(\bar{\bar{\tau}} : \bar{\bar{\tau}})} = \sqrt{\frac{1}{2}(\tau_{zz}^2 + \tau_{rr}^2 + \tau_{\theta\theta}^2 + 2\tau_{rz}^2)} = 16.664$. The pressure gradient is constant along the $r$-direction $\frac{dP}{dz} = -\frac{a}{Ws\sqrt{\xi(2-\xi)}} = -7.395$.

The FBC at the inflow involves calculation of the integral according to Eq. (40). Our tests showed that in this simple problem our scheme works equally well with the scheme proposed by Dimakopoulos et al. [22]. The results for $Ws = 0.1$ and $\xi = 0.5$ are given in Fig. 3 for the contours of various flow variables, which are the stream function $\psi$, the axial velocity $u_z$, the pressure $P$, the normal stresses $\tau_{zz}$ and $\tau_{rr}$, and the shear stress, $\tau_{rz}$. The contours here and

in the following are given as 11 equidistant lines between the minimum and maximum values (not shown). Thus, for the stream function $\psi$ the minimum value is 0 and the maximum value is 1, while the contour interval is $\Delta\psi = 1/10 = 0.1$. We observe that all contours (except the pressure) are perfectly parallel to the flow, as they should, since this is a fully-developed shear flow. The pressure contours (isobars) show the distinct curvature associated with a non-zero $N_2$. When $N_2 = 0$, the isobars are perfectly vertical.

Fig. 4 shows the corresponding radial distributions (axial velocity and the three stresses) for $Ws = 0.1$ and $\xi = 0.5$. The results are shown at the inlet but they are identical for any cut along the domain. Also the numerical solution faithfully reproduces the analytical solutions of Eq. (44).

Fig. 5 shows the axial pressure distributions for $Ws = 0.1$ and $\xi = 0$ or $\xi = 0.5$. In both cases, the axial pressure distribution is linear. However, when $\xi = 0$, the axial pressure distribution along the wall and the centerline coincide. When $\xi \neq 0$, there is a radial distribution of pressure, which is quadratic in $r$, and the results between the wall and the centerline are different. In both cases, the numerical results agree exactly with the analytical solutions of Eq. (44) either by using the fully-developed profiles at entry and/or exit or the FBC.

It is interesting to note that the upper limits for convergence were different for $\xi = 0$ and $\xi \neq 0$. In the former case, no upper limit was found even for $Ws = 10^{+5}$. In the latter case, an upper limit was found for $Ws = 0.175$ with $\xi = 0.5$. These limits are not related to the imposition of the FBC, since they are also found when imposing a fully developed velocity profile at the inlet.

### 4.2. Flow in an annular die (Test #2)

The next numerical test is made for a viscous or viscoelastic fluid flowing under pressure through an annular (axisymmetric) tapered die used in industrial operations [35]. The details of the die design are given in Fig. 6. The dimensions have been scaled with the outer radius $R_0 = 0.15$ cm at exit. The straight annular channel has a channel gap $r_o - r_i = H = 0.5$, where $r_o$ is the outer radius and $r_i$ is the inner radius. The problem has been solved before without the FBC, by applying as inlet boundary conditions a fully-developed velocity profile corresponding to a given apparent shear rate of $\dot{\gamma}_A$, i.e., $u_z = f(r)$ and $u_r = 0$, and a constant temperature profile $T = T_0$; at the outlet the boundary conditions were: surface traction $\overline{T} = 0$ and heat flux $\bar{q} = 0$. Along the solid walls ABC and FED either zero velocities are imposed or a slip law (see below). When using the N–R scheme we have to set a datum pressure and so we have decided to set the pressure equal to zero at one node (D). On the other hand, for the P scheme no datum pressure should be imposed and this was found to be essential when applying the FBC [13]. The problem is solved again here by applying at inlet and outlet the FBC as shown in Fig. 6.

The FBC at the inflow involves calculation of the integral according to Eq. (40). Our tests showed that the best results (in terms of smoothness of the profiles) are obtained when choosing a node as close as possible to the position of the maximum velocity in the principal direction of the flow. In some cases one knows that position *a priori* (e.g., the axis of symmetry for the Poiseuille flow in a cylindrical pipe). Sometimes, however, things are not so simple and there are cases where it is quite difficult, if not impossible, to predict beforehand the exact position of the maximum velocity. This is also the case for flow inside an annular die. Our tests have revealed that it is adequate to simply impose Eq. (40) at a node fairly close to the position that one would expect the maximum velocity to arise. For the purposes of our test we have decided to select the middle element at inlet and impose the flow rate at the upper node along its side (see also Fig. 1).

Details about the mesh characteristics (number of elements, nodes, dof) that we have used are given in Table 1. First we present results for a Newtonian fluid with a mean outlet velocity $u_{z,m} = 1$ for ease of calculations and for easy checking by others. The results employing the FBC are shown in Fig. 7 as contours of the two velocity components $u_z$ and $u_r$ (Fig. 7a and b) and isobars P (Fig. 7c). The results show a nice smooth parallel flow to the channel walls all the way from the inlet to the outlet, while the isobars are normal to the flow.

Another test to examine the behavior of the FBC is to compare the solution from the full domain (long) with a truncated domain (short) starting at $z = 25$ and applying at the inlet the FBC. The radial profiles of $u_z$, $u_r$, $p$ for both cases are shown in Fig. 8. In both cases, the FBC is used at the domain inflow. The velocity and pressure profiles of Fig. 8 aptly show that the results from the short domain match very well those from the long one. Only the pressure profile is shifted by a constant corresponding to the reduced length $z = 25$. Similar behavior was obtained at any cut downstream. There is some discrepancy in the element where the flow rate condition was imposed (Eq. (40)). This is the element in the middle of the channel, where the maximum velocity occurs. Our testing showed that this behavior grows worse as we choose elements near the walls and improves as we get closer to the position of the maximum velocity in the $z$-direction. To get optimum results we could always apply a trial-and-error algorithm in order to evaluate the position of the maximum velocity and apply Eq. (40) at that node.

Similar results were obtained when using the viscoelastic PTT model of Eqs. (15)–(18). Corresponding results are shown for $Ws = 0.1$ with a non-zero second normal-stress difference assumed ($\xi = 0.1$). The contours for the two velocities and the isobars as well as the velocity vectors are shown in Fig. 9 near the inlet at the short domain set at $z = 25$. The corresponding velocity and pressure radial profiles (short) are shown in Fig. 10 and compared with those obtained from the full domain (long) at the same axial position. The results are again smooth and they match closely those obtained from the long domain. Only the pressure profile is shifted by a constant corresponding to the reduced length $z = 25$. The pressure contours and profiles show curvature reflecting the fact that a non-zero second normal-stress difference has been assumed ($\xi = 0.1$). Furthermore, the same good behavior is also obtained for the four viscoelastic stresses, as shown in Fig. 11. Namely, the axial normal stress $\tau_{zz}$ (Fig. 11a), the radial normal stress $\tau_{rr}$ (Fig. 11b), the shear stress $\tau_{rz}$ (Fig. 11c), and the azimuthal normal stress $\tau_{\theta\theta}$ (Fig. 11d). Therefore, this example is another good manifestation of the efficiency of FBC applied in a flow domain cut at some arbitrary distance upstream.

It should be noted that when we post-process the results of our simulation and solve Eq. (30) to get the streamlines, it is also important to apply the FBC to the Poisson equation for the stream function, since the integral of Eq. (39) is not zero due to the inclined flow.

We turn now our attention to real data of the process for a fluoro-ethylene polymer melt (FEP), which is used in annular dies for coating purposes [35]. The flow process is now considered creeping ($Re \approx 0$), viscous, non-isothermal, weakly compressible, with material data listed in Table 2. The viscosity of the melt obeys the Cross model (Eq. (11)) with data listed in Table 3. Furthermore, the material slips at the wall according to a power law:

$$a_T u_{sl} = -\beta_{sl}\sigma_w^b, \tag{46}$$

where $a_T$ is given by Eq. (13), $u_{sl}$ is the slip velocity, $\sigma_w$ is the shear stress at the wall, and the constants $\beta_{sl}$ and $b$ are listed in Table 2. The walls are kept isothermal at $T_0 = 371$°C. The apparent shear rate was calculated by using the formula [35]:

$$\dot{\gamma}_A = \frac{6Q}{0.25(D-d)^2 0.5\pi(D+d)}, \quad (47)$$

where $Q$ is the volumetric flow rate, $d$ and $D$ are the tip (inner) and die (outer) diameters ($d = 0.15$ cm and $D = 0.3$ cm), respectively. The apparent shear rates ranged from 80 to 5600 $s^{-1}$. Here we present results for a test run at the highest apparent shear rate of 5600 $s^{-1}$. In this case, the dimensionless numbers are: $Re = 1.89 \times 10^{-3}$, $B_c = 3.57 \times 10^{-4}$, $B_p = 1.13 \times 10^{-2}$, $B_{sl} = 0.821$, $Pe = 2859$, $Na = 10.89$. They indicate a creeping flow with weak compressibility, weak pressure-dependence of viscosity, strong slip, strong thermal convection, and moderate viscous dissipation, respectively.

Fig. 12 shows the results by applying as inflow boundary conditions a plug velocity profile and a constant temperature profile. The results are not smooth and show some disturbances, which of course are smoothed out further downstream (for this case within one to two gaps because the flow is very slow at inlet). However, in other cases of strong convective flows or viscoelastic flows, this smoothing out may take much longer to develop.

Fig. 13 shows the corresponding results when applying the FBC at the inflow. The inlet element chosen for the imposition of the flow rate (Eq. (40)) was two elements below the middle one, due to the appearance of the maximum velocity at this node, taking into account that severe slip is also present at both walls. Now all results are smooth and coincide with results obtained from a much longer domain upstream. Thus, even for the case of non-isothermal, weakly compressible flows with slip at the wall, the FBC works well and gives nice and smooth profiles at the inflow as well as the outflow.

A more detailed view of the differences between the arbitrary 1-D profiles and the ones obtained by applying the FBC is shown in Fig. 14 for the radial inlet profiles of the primary variables, velocities-pressure–temperature. The 1-D velocity profile imposed is a plug velocity profile for $u_z$, whereas the FBC gives a nice smooth curved profile with different slip velocities at the two annular walls (Fig. 14a). The profile for $u_r$ from FBC is like the $u_z$-profile but with negative values, while the 1-D profile for $u_r$ is zero (Fig. 14b). The pressure profile obtained from FBC is a straight line, while the 1-D solution gives a curved one (Fig. 14c). However, the differences in absolute numbers are not big (being about 17 MPa). The same is true for the inlet temperature profiles (Fig. 14d), where a constant temperature is assumed at 371 °C for the 1-D solution, while the FBC provides the characteristic profile with the two hills close to the walls and one valley in the middle, due to a viscous flow with important viscous dissipation effects ($Na > 1$). Again, due to the big channel at the inlet and the slow flow there, the temperature differences are in the order of 0.02 °C, which of course are negligible. This in essence justifies the imposition of a constant temperature profile that has been used in the past in the non-isothermal simulations of polymer processing [35]. However, there may be cases where such an approximation is not appropriate, and the application of the FBC at the inlet may prove extremely valuable.

Lastly, we would like to add that the above run has also been done with the K-BKZ integral viscoelastic model [15,35] but that due to the nature of this FEP melt, viscoelasticity is not important due to severe slip effects, and the results are not too much affected. Thus, we do not show these results here (see details in [35] without the FBC at inlet).

## 5. Conclusions

The Free (Open) Boundary Condition (FBC, OBC) has been applied at inflow boundaries with the purpose of testing its applicability in various flow problems and with programs employing either the Newton–Raphson (N–R) iterative scheme or a direct substitution scheme (Picard iteration). The extra equation needed is the imposition of a known flow rate given as the integral of the unknown *a priori* velocity profile. It is remarkable that the only information needed for this is the basis (shape) functions of the inlet finite elements, which are used in the calculation of the flow rate.

Three test cases have been examined for Newtonian/Generalized Newtonian and non-Newtonian viscoelastic fluids obeying the Phan–Thien/Tanner model. The test cases include the simple Poiseuille flow in a tube, while the other two cases refer to axisymmetric annular flows in tapered dies, where the inflow boundary condition is not trivial. Effects studied include non-isothermal flows, with slip at the wall, weak compressibility, and temperature-, pressure- and strain-rate dependence of the viscosity. In all cases, the FBC gives an inlet profile, which is an extrapolation of the full flow field to the boundary, and thus it matches profiles obtained from an artificial long entrance where usually only the flow rate is imposed and the flow field is left to develop itself. Furthermore, the FBC at inlet does not affect the upper limits of convergence for viscoelastic flows (the HWNP) and is also valid for high $Re$ number flows as shown in [22].

The present results are offered as reference solutions for researchers working with the numerical simulation of fluid flows. The current implementation of the FBC is then a very attractive alternative for imposing inflow boundary conditions in all cases of fluid flow, and in particular when there is uncertainly of what is happening at an artificial inflow boundary. Furthermore, its 3-D implementation is straight-forward and certainly very helpful in reducing the computing effort and computational cost by using shorter domains artificially cut at inlet and outlet.

## Acknowledgements

E.M. would like to acknowledge the financial support by the "THALES" project of the Ministry of Education, Greece. G.K. would like to acknowledge the financial support by the General Secretariat of Research and Technology of Greece under the Action "Supporting Postdoctoral Researchers" (Grant No: PE8(906)), co-funded by the European Social Fund and National Resources.

## References

[1] T.C. Papanastasiou, N. Malamataris, K. Ellwood, A new outflow boundary condition, Int. J. Numer. Meth. Fluids 14 (1992) 587–608.
[2] R.L. Sani, P.M. Gresho, Résumé and remarks on the open boundary condition minisymposium, Int. J. Numer. Meth. Fluids 18 (1994) 983–1008.
[3] D.K. Gartling, A test problem for outflow boundary conditions – flow over a backward-facing step, Int. J. Numer. Meth. Fluids 11 (1990) 953–967.
[4] J.M. Leone Jr., Open boundary condition symposium benchmark solution: stratified flow over a backward-facing step, Int. J. Numer. Meth. Fluids 11 (1990) 969–984.
[5] N.G. Malamataris, Computer-aided analysis of flow on moving and unbounded domains: phase-change fronts and liquid leveling, Ph.D. dissertation, The University of Michigan, 1991.
[6] N.T. Malamataris, T.C. Papanastasiou, Unsteady free surface flows on truncated domains, Ind. Eng. Chem. Res. 30 (1991) 2211–2219.
[7] D.F. Griffiths, The 'no boundary condition' outflow boundary condition, Int. J. Numer. Meth. Fluids 24 (1997) 393–411.
[8] M. Renardy, Imposing no boundary condition at outflow: why does it work?, Int J. Numer. Meth. Fluids 24 (1997) 413–417.
[9] M.M. T Wang, T.W.H. Sheu, Implementation of a free boundary condition to Navier–Stokes equations, Int. J. Numer. Meth. Heat Fluid Flow 7 (1997) 95–111.
[10] S.J. Park, S.J. Lee, On the use of the open boundary condition method in the numerical simulation of nonisothermal viscoelastic flow, J. Non-Newton. Fluid Mech. 87 (1999) 197–214.
[11] K.B. Sunwoo, S.J. Park, S.J. Lee, K.H. Ahn, S.J. Lee, Numerical simulation of three-dimensional viscoelastic flow using the open boundary condition method in coextrusion process, J. Non-Newton. Fluid Mech. 99 (2001) 125–144.
[12] Y. Dimakopoulos, J. Tsamopoulos, On the gas-penetration in straight tubes completely filled with a viscoelastic fluid, J. Non-Newton. Fluid Mech. 117 (2004) 117–139.
[13] E. Mitsoulis, N.A. Malamataris, Free (open) boundary condition (FBC) revisited: some experiences with viscous flow problems, Int. J. Numer. Meth. Fluids 68 (2012) 1299–1323.

[14] E. Mitsoulis, N.A. Malamataris, The free (open) boundary condition (FBC) in viscoelastic flow simulations, Int. J. Mater. Form. (2012), http://dx.doi.org/10.1007/s12289-011-1071-6.
[15] E. Mitsoulis, N.A. Malamataris, The free (open) boundary condition with integral constitutive equations, J. Non-Newton. Fluid Mech. 177–178 (2012) 97–108.
[16] E. Mitsoulis, Annular extrudate swell of pseudoplastic and viscoplastic fluids, J. Non-Newton. Fluid Mech. 141 (2007) 138–147.
[17] G. Karapetsas, J. Tsamopoulos, Steady extrusion of viscoelastic materials from an annular die, J. Non-Newton. Fluid Mech. 154 (2008) 136–152.
[18] V. Gravemeier, A. Comerford, L. Yoshihara, M. Ismail, W.A. Wall, A novel formulation for Neumann inflow boundary conditions in biomechanics, Int. J. Numer. Meth. Biomed. Eng. 28 (2012) 560–573.
[19] S. Annerel, J. Degroote, T. Claessens, P. Segers, P. Verdonck, J. Vierendeels, The upstream boundary condition influences the leaflet opening dynamics in the numerical FSI simulation of an aortic BMHV, Int. J. Numer. Meth. Biomed. Eng. (2012), http://dx.doi.org/10.1002/cnm2470.
[20] D.G. Baird, D.I. Collias, Polymer Processing: Principles and Design, Butterworth-Heinemann, Boston, MA, 1995.
[21] Z. Tadmor, C.G. Gogos, Principles of Polymer Processing, second ed., SPE Monograph Series, Wiley, New York, 2006.
[22] Y. Dimakopoulos, A.C. Bogaerds, P.D. Anderson, M.A. Hulsen, F.P.T. Baaijens, Direct numerical simulation of a 2D-stented aortic heart valve at physiological flow rates, Comput. Meth. Biomech. Biomed. Eng. (2011), http://dx.doi.org/10.1080/10255842.2011.581238.
[23] R.I. Tanner, Engineering Rheology, second ed., Oxford University Press, Oxford, 2000.
[24] R.B. Bird, R.C. Armstrong, O. Hassager, Dynamics of Polymeric Liquids, Fluid Mechanics, second ed., vol. I, Wiley, New York, 1987.
[25] T.C. Papanastasiou, Flow of materials with yield, J. Rheol. 31 (1987) 385–404.
[26] A. Hannachi, E. Mitsoulis, Sheet coextrusion of polymer solutions and melts: comparison between simulation and experiments, Adv. Polym. Technol. 12 (1993) 217–231.
[27] G. Karapetsas, J. Tsamopoulos, Steady extrusion of viscoelastic materials from an annular die, J. Non-Newton. Fluid Mech. 154 (2008) 136–152.
[28] E. Mitsoulis, Annular extrudate swell of Newtonian fluids: effects of compressibility and slip at the wall, ASME J. Fluids Eng. 129 (2007) 1384–1393.
[29] E. Mitsoulis, Annular extrudate swell of Newtonian fluids revisited: extended range of compressible simulations, ASME J. Fluids Eng. 131 (2009). 071203-1-10.
[30] D. Rajagopalan, R.C. Armstrong, R.A. Brown, Finite element methods for calculation of steady, viscoelastic flow using constitutive equations with Newtonian viscosity, J. Non-Newton. Fluid Mech. 36 (1990) 159–192.
[31] R.A. Brown, M.J. Szady, P.J. Northey, R.C. Armstrong, On the numerical stability of mixed finite-element methods for viscoelastic flows governed by differential constitutive equations, Theor. Comput. Fluid Dyn. 5 (1993) 77–106.
[32] A.N. Brooks, T.J.R. Hughes, Streamline upwind/Petrov–Galerkin formulations for convection dominated flows with particular emphasis on the incompressible Navier–Stokes equations, Comput. Meth. Appl. Mech. Eng. 32 (1982) 199–259.
[33] R. Keunings, On the high Weissenberg number problem, J. Non-Newton. Fluid Mech. 20 (1986) 209–226.
[34] M.A. Alves, F.T. Pinho, P.J. Oliveira, Study of steady pipe and channel flows of a single-mode Phan–Thien–Tanner fluid, J. Non-Newton. Fluid Mech. 101 (2001) 55–76.
[35] E. Mitsoulis, S.G. Hatzikiriakos, Tubing extrusion of a fluoropolymer melt, Intern. Polym. Proc. 27 (2012) 259–269.